

FACULTEIT TOEGEPASTE WETENSCHAPPEN
DEPARTEMENT ELEKTROTECHNIEK
ESAT - TELEMIC
KARDINAAL MERCIERLAAN 94
B-3001 HEVERLEE
BELGIUM



KATHOLIEKE
UNIVERSITEIT
LEUVEN

REPORT

OUR REFERENCE
HEVERLEE, August 1997

An X-Band High-Gain Dielectric Rod Antenna

Serge Y. Stroobandt

1 Introduction

Today's wireless technology shows a significant shift towards millimeter-wave frequencies. Not only does the lower part of the electromagnetic spectrum become saturated, mm-wave frequencies allow for wider bandwidths and high-gain antennas are physically small. Millimeter-waves also offer a lot of benefits for radar applications, such as line-of-sight propagation and a higher imaging resolution. Beams at these frequencies are able to penetrate fog, clouds and smoke 20 to 50 times better than infra-red beams.

At millimeter-wave frequencies, dielectric rod antennas provide significant performance advantages and are a low cost alternative to free space high-gain antenna designs such as Yagi-Uda and horn antennas, which are often more difficult to manufacture at these frequencies [1]. Not surprisingly, the dielectric rod antenna is also nature's favourite choice when it comes to nanometer-wave applications: the retina of the human eye is an array of more than 100 million dielectric antennas (both rods and cones) [2], [3] and [4]. Furthermore, the degree of mutual coupling is limited in typical array applications.

The relatively infrequent use of dielectric antennas is due in part to the lack of adequate design and analysis tools. Lack of analysis tools inhibits antenna development because designers must resort to cut-and-try methods. It is only recently that simulation of electromagnetic fields in arbitrarily shaped media has become fast and practical. Simulation results of a body of revolution (BoR) FDTD computer code have been reported in reference [1]. However, for the present work, no simulation code was available at K. U. Leuven - TELEMIC.

The aim of this report is to demonstrate the relative ease of obtaining high-gain and broad-band performance from dielectric rod antennas that are at the same time easy and cheap to construct. The fundamental working principles of the dielectric rod antenna are explained, as well as their relation to other surface wave antennas; like there are the Yagi-Uda antenna, the cigar antenna and the stacked patch antenna. A prototype of an X-band dielectric rod antenna has been designed and measured. The antenna was designed at X-band because waveguide and measuring equipment was available for this band. Finally, results and areas for improvement are also discussed.

2 Designing a Dielectric Rod Antenna

2.1 Radiation Mechanisms of the Dielectric Rod Antenna

The dielectric rod antenna belongs to the family of surface wave antennas. The propagation mechanisms of surface waves along a dielectric and/or magnetic rod are explained in Appendices A and B. The hybrid HE_{11} mode (Fig. B.2) is the dominant surface wave mode and is used most often with dielectric rod antennas. The higher, transversal modes TE_{01} and TM_{01} produce a null in the end-fire direction or are below cut-off. The HE_{11} mode is a slow wave (i.e. $\beta_z > k_1$) when the losses in the rod material are small. In this case, increasing the rod diameter will result in an even slower HE_{11} surface wave of which the field is more confined to the rod.

The dielectric or magnetic material could alternatively be an artificial one, e.g., a series of metal disks or rods (i.e. the cigar antenna and the long Yagi-Uda antenna, respectively). Design information for the long Yagi-Uda antenna will be employed for the design of the dielectric rod antenna. Both structures are shown in Figure 1.

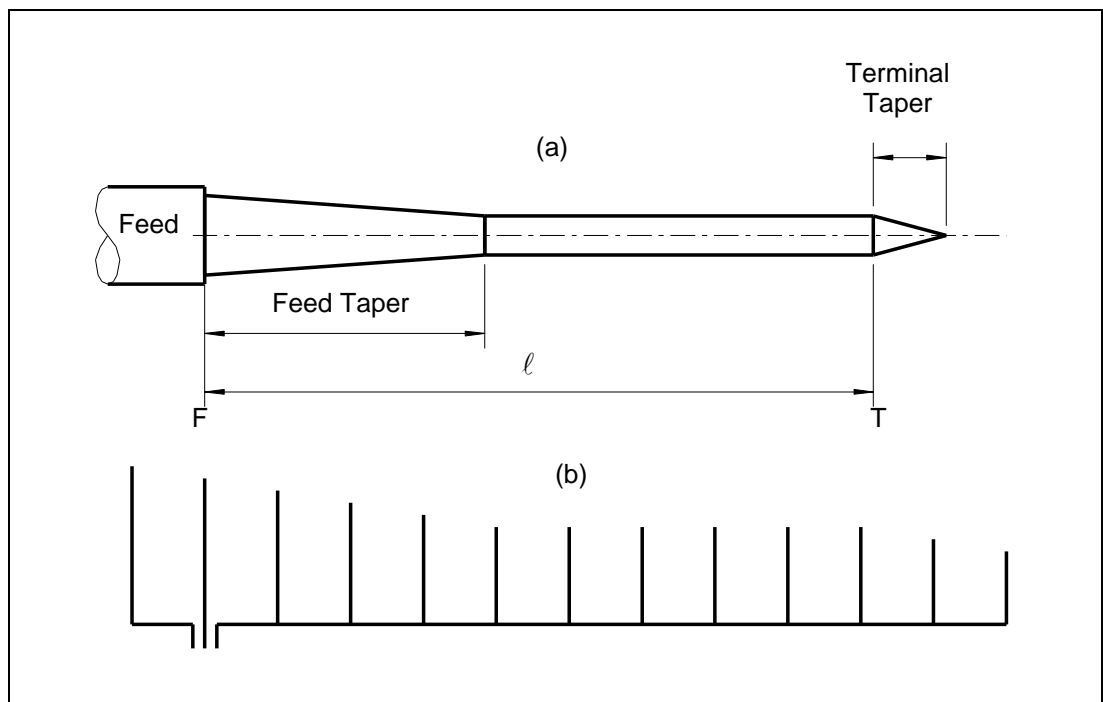


Figure 1: Two surface wave antenna structures: the dielectric/magnetic rod antenna (a) and the long Yagi-Uda antenna (b)

Since a surface wave radiates only at discontinuities, the total pattern of this antenna (normally end-fire) is formed by interference between the feed and terminal patterns [5, p. 1]. The feed F (consisting of a circular or rectangular waveguide in Figure 1a and a monopole and a reflector in Figure 1b) couples a portion of the input power into a surface wave, which travels along the antenna structure to the termination T, where it radiates into space. The ratio of power in the surface wave to the total input power is called *the efficiency of excitation*. Normally, its value is between 65 and 75 percent. Power not coupled into the surface wave is directly radiated by the feed in a pattern resembling that radiated by the feed when no antenna structure is in front of it [5, p. 9].

The tapered regions in Figure 1 serve different purposes. *The feed taper* increases the efficiency of excitation and also affects the shape of the feed pattern. *A terminal taper* reduces the reflected surface wave to a negligible value. A reflected surface wave would spoil the radiation pattern and bandwidth of the antenna. *A body taper* (not shown) suppresses sidelobes and increases bandwidth.

2.2 Designing for Maximum Gain

2.2.1 Field Distribution along a Surface Wave Antenna

The field distribution along a surface wave antenna is depicted in Figure 2. The graph shows a hump near the feed. The size and extent of the hump are a function of feed and feed taper construction. The surface wave is well established at a distance l_{\min} from the feed where the radiated wave from the feed, propagating at the velocity of light, leads the surface wave by about 120° [5, p. 10]:

$$l_{\min} \beta_z - l_{\min} k_0 = \frac{\pi}{3}. \quad (1)$$

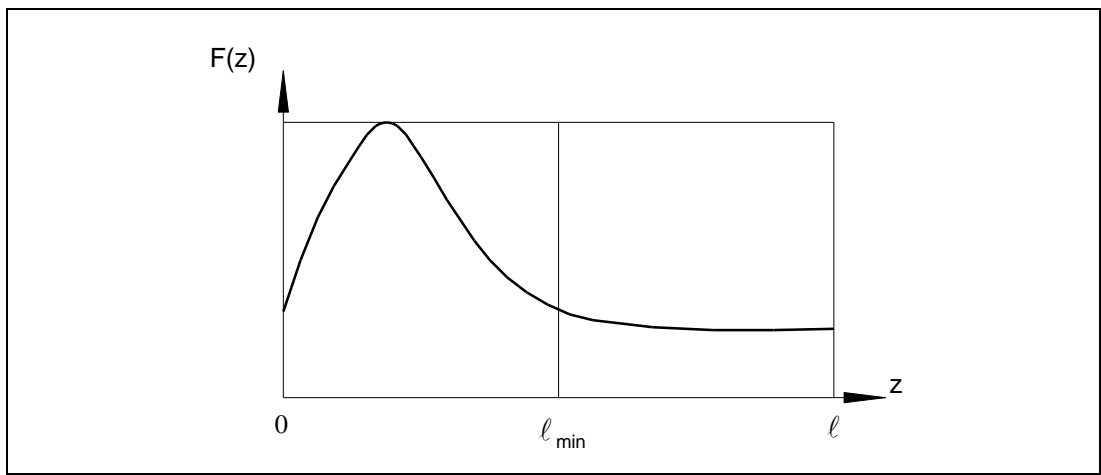


Figure 2: Amplitude of the field along a surface wave antenna

The location of l_{\min} on an antenna designed for maximum gain is seen in Figure 2 to be about halfway between the feed and the termination. Since the surface wave is fully developed from this point on, the remainder of the antenna length is used solely to bring the feed and terminal radiation into the proper phase relation for maximum gain.

The phase velocity along the antenna and the dimensions of the feed and terminal tapers in the maximum gain design of Figure 1a must now be specified.

2.2.2 The Hansen-Woodyard Condition: Flat Field Distribution

If the amplitude distribution in Figure 2 were flat, maximum gain would be obtained by meeting the Hansen-Woodyard condition (strictly valid for antenna lengths $\ell \gg \lambda_0$), which requires the phase difference at T between the surface wave and the free space wave from the feed to be approximately 180° :

$$\ell\beta_z - \ell k_0 = \pi \Rightarrow \frac{\lambda_0}{\lambda_z} = 1 + \frac{\lambda_0}{2\ell}, \quad (2)$$

which is plotted as the upper dashed line in Figure 3.

2.2.3 100% Efficiency of Excitation

If the efficiency of excitation were 100%, there would be no radiation from the feed. Consequently, there would be no interference with the terminal radiation and the antenna needs to be just long enough so that the surface wave is fully established; that is $\ell = \ell_{\min}$ in Figure 2.

$$\text{From equation (1): } \ell\beta_z - \ell k_0 = \pi \Rightarrow \frac{\lambda_0}{\lambda_z} = 1 + \frac{\lambda_0}{6\ell}, \quad (3)$$

which is plotted as the lower dashed line in Figure 3.

2.2.4 Ehrenspeck and Pöhler: Yagi-Uda without Feed Taper

Ehrenspeck and Pöhler [6] have determined experimentally the optimum terminal phase difference for long Yagi-Uda antennas without feed taper, resulting in the solid curve of Figure 3. Note that in the absence of a feed taper, ℓ_{\min} occurs closer to F and the hump is higher. Because feeds are more efficient when exciting slow surface waves than when the phase velocity is closer to that of light, the solid line starts near the 100% excitation efficiency line and ends near the line for the Hansen-Woodyard condition.

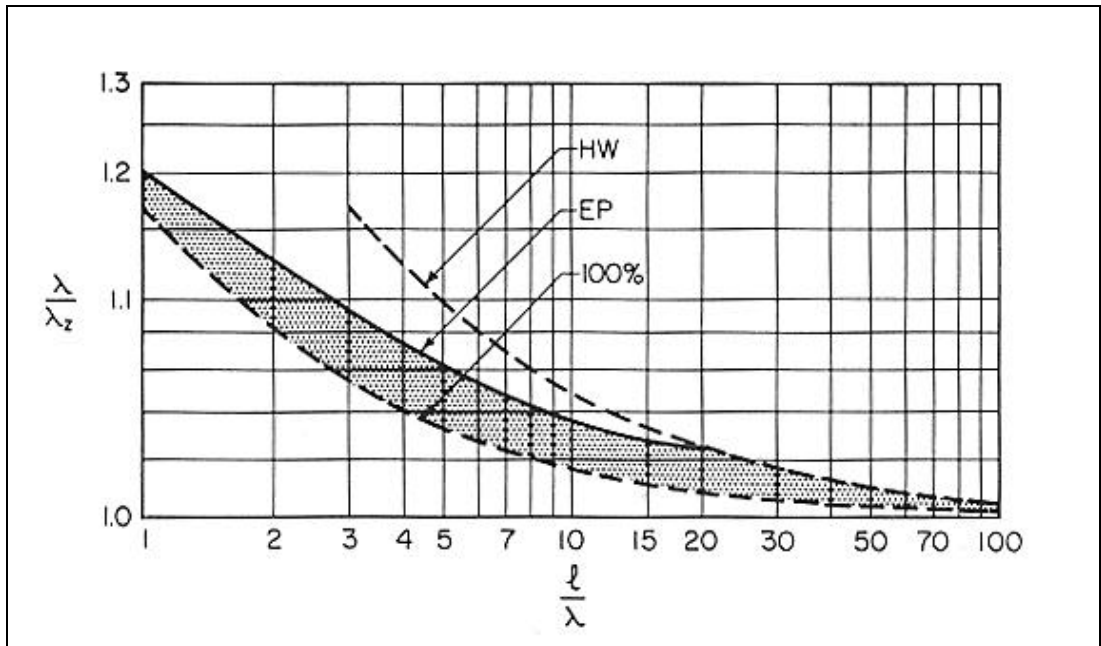


Figure 3: Relative phase velocity for maximum gain as a function of relative antenna length [5, p. 12] (HW: Hansen-Woodyard condition; EP: Ehrenspeck and Pöhler experimental values; 100%: 100% efficiency of excitation)

2.2.5 The Actual Design

In practice, the optimum terminal phase difference for a prescribed antenna length cannot easily be calculated because the size and extent of the hump in Figure 2 are a function of feed and feed taper construction. When a feed taper is present, the optimum λ_0/λ_z values must lie in the shaded region of Figure 3. Although this technique for maximizing the gain has been strictly verified only for long Yagi-Uda antennas, data available in literature on other surface wave antenna structures suggest that the optimum λ_0/λ_z values lie on or just below the solid curve in all instances [5, p. 11].

It follows from Figure 3 that for maximum excitation efficiency a feed taper should begin at F with λ_0/λ_z between 1.2 and 1.3. It is common engineering practice to have the feed taper extending over approximately 20% of the full antenna length [5, p. 12].

The terminal taper should be approximately half a (surface wave) wavelength long to match the surface wave to free space.

Thus far, only the relative phase velocity has been specified as a function of relative antenna length. However, nothing has yet been said about what the actual antenna length should be. As can be seen from Figure 4, the gain and the beamwidth of a surface wave antenna are determined by the relative antenna length. Figure 4 is based on the values of maximum gain reported in literature.

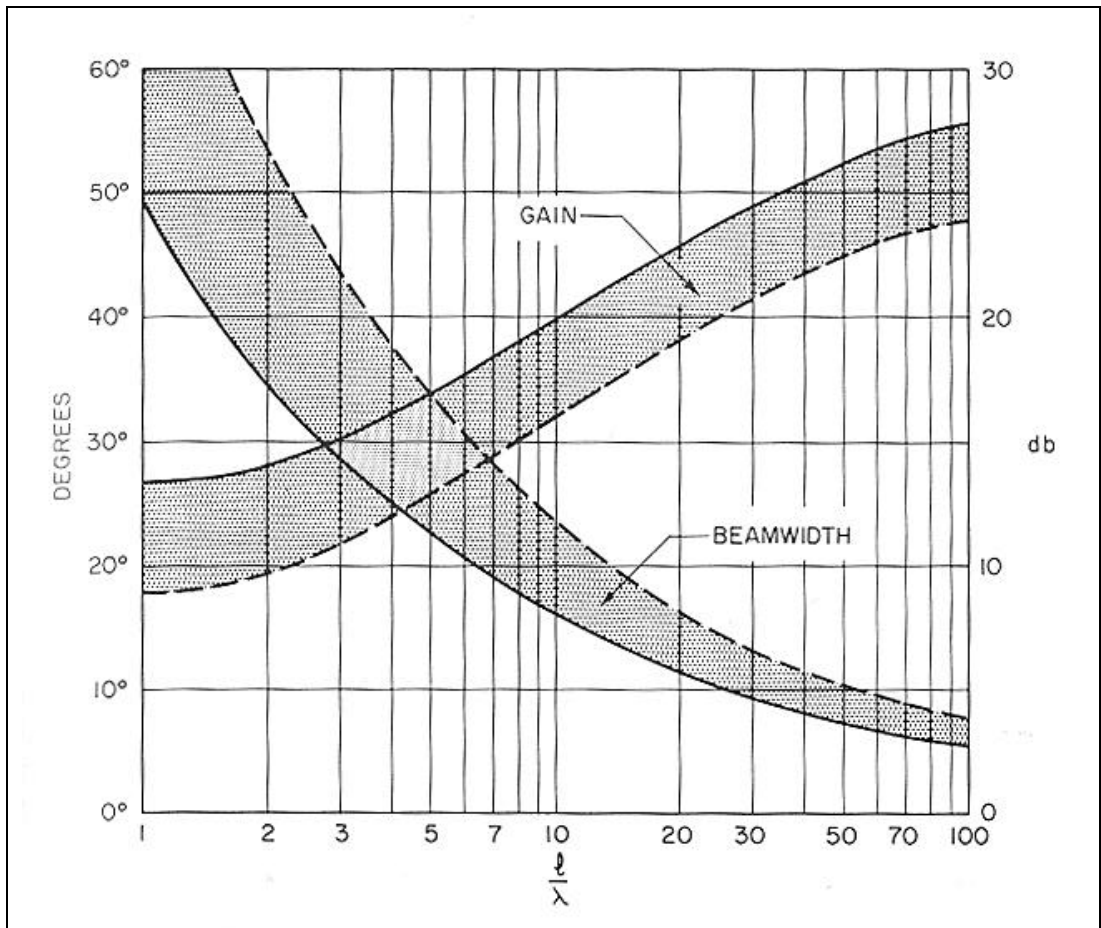


Figure 4: Gain and beamwidth of a surface wave antenna as a function of relative antenna length. Solid lines are optimum values; dashed lines are for low-sidelobe and broad-band designs [5, p. 13].

The gain of a long ($l \gg \lambda_0$) uniformly illuminated (no hump in Figure 2) end-fire antenna whose phase velocity satisfies equation (2), was shown by Hansen and Woodyard to be approximately

$$G_{\max} \approx \frac{7l}{\lambda_0}.$$

As Figure 4 shows, the gain is higher for shorter antennas. This is due to the higher efficiency of excitation and the presence of a hump in Figure 2.

The antenna presented in this work is designed for a maximum gain of $G_{\max} = 100 = 20\text{dBi}$ and an operating frequency of 10.4GHz ($\lambda_0 = 28.8\text{mm}$).

As can be seen from Figure 4, this corresponds to an antenna length of $10\lambda_0$ or $l = 288\text{mm}$. Surface wave antennas longer than $20\lambda_0$ are difficult to realize due to poor excitation efficiency at their feed. Also, the longer the antenna, the faster the surface wave and the more the surface wave field extends out of the dielectric.

The length of the feed taper should be one fifth of the antenna length or 57.6mm.

The optimum terminal phase difference is the only design parameter that needs to be determined empirically if no information is available on the excitation efficiency of the feed. A general expression for the optimal terminal phase difference can be obtained from equations (2) and (3)

$$\frac{\lambda_0}{\lambda_z} = 1 + \frac{\lambda_0}{p\ell}, \quad (4)$$

where

$p = 2$ for the Hansen-Woodyard condition and
 $p = 6$ in the case of 100% efficiency of excitation.

The optimum terminal phase difference with 100% efficiency of excitation is, by virtue of (3),

$$\left. \frac{I_0}{I_z} \right|_{100\%} = 1.01667, \text{ which corresponds to } p = 6.$$

The optimum terminal phase difference in absence of a feed taper is (Figure 3)

$$\left. \frac{I_0}{I_z} \right|_{EP} = 1.02764, \text{ which corresponds to } p = 3.618.$$

For this design the terminal phase difference is chosen to equal the average of these two values or

$$\frac{\lambda_0}{\lambda_z} = 1.022, \text{ which corresponds to } p = 4.545.$$

The terminal taper length should be about $\lambda_z/2 \approx 15\text{mm}$.

The only parameters that are left to be determined are the rod material and the rod diameter, which is a function of the material parameters. The rod material should have low values for its relative permittivity and permeability. High values would result in an impractical small rod diameter. Other material requirements are: small dielectric and magnetic losses, weather-proof (especially UV-proof) and high rigidity (do not forget that the present antenna will be more than 30cm long). Only polystyrene and ferrites meet the above-mentioned requirements. Surface wave antennas build out of polystyrene are sometimes called polyrod antennas, whereas those out of ferrite are also known as ferrod antennas. Polystyrene (Polypenco Q200.5) is chosen for this design. Figure 5 gives the relative phase velocity of the first three surface wave modes along a polystyrene rod. The graphs are obtained by solving the dispersion equation (B.16) of Appendix B.

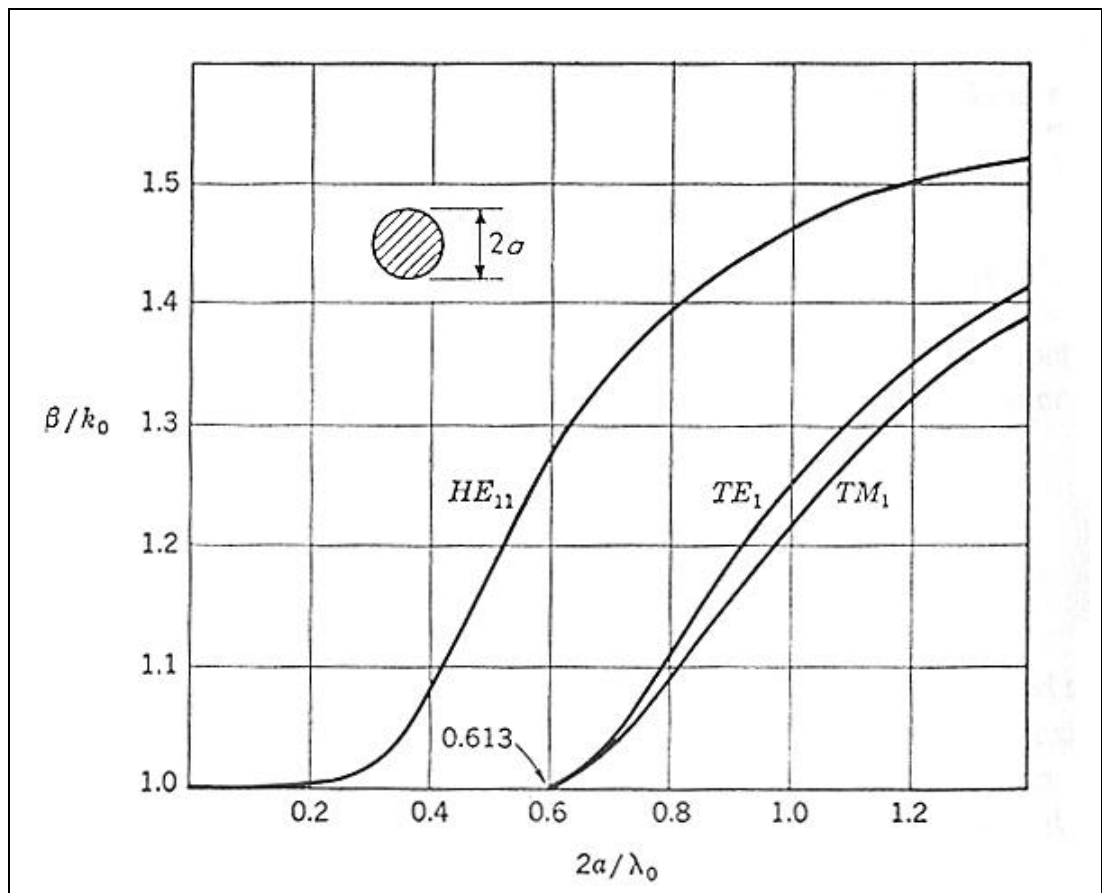


Figure 5: Ratio of β_z/k_0 (or equivalently, λ_0/λ_z) for the first three surface wave modes on a polystyrene rod ($\epsilon_{r1} = 2.55$) [7, p. 722]

A rod diameter $2a = 8.02\text{mm}$ results in the desired relative phase velocity of $\beta_z/k_0 = \lambda_0/\lambda_z = 1.022$.

To improve the excitation efficiency, the initial rod diameter is chosen to be 16.4mm , which corresponds to a relative phase difference of $\beta_z/k_0 = \lambda_0/\lambda_z = 1.250$.

The surface wave antenna structure is now fully specified. Engineering drawings can be found later in this chapter. The design of the feed is discussed in the next section.

2.3 The Feed

The most practical feed is a rectangular waveguide, especially if it is the intention to excite the antenna in linear polarization. In this design, the aperture width of an X-band waveguide is reduced to 12.874mm in order to increase the excitation efficiency (see also engineering drawings on the following pages). The height of the X-band waveguide remains 10.160mm. Part of the dielectric rod is accommodated by the waveguide aperture to provide improved electromagnetic coupling and mechanical support. The cut-off frequency of the dominant TE₁₀ mode of the reduced-sized filled rectangular waveguide is checked now and found to be sufficiently low for this application:

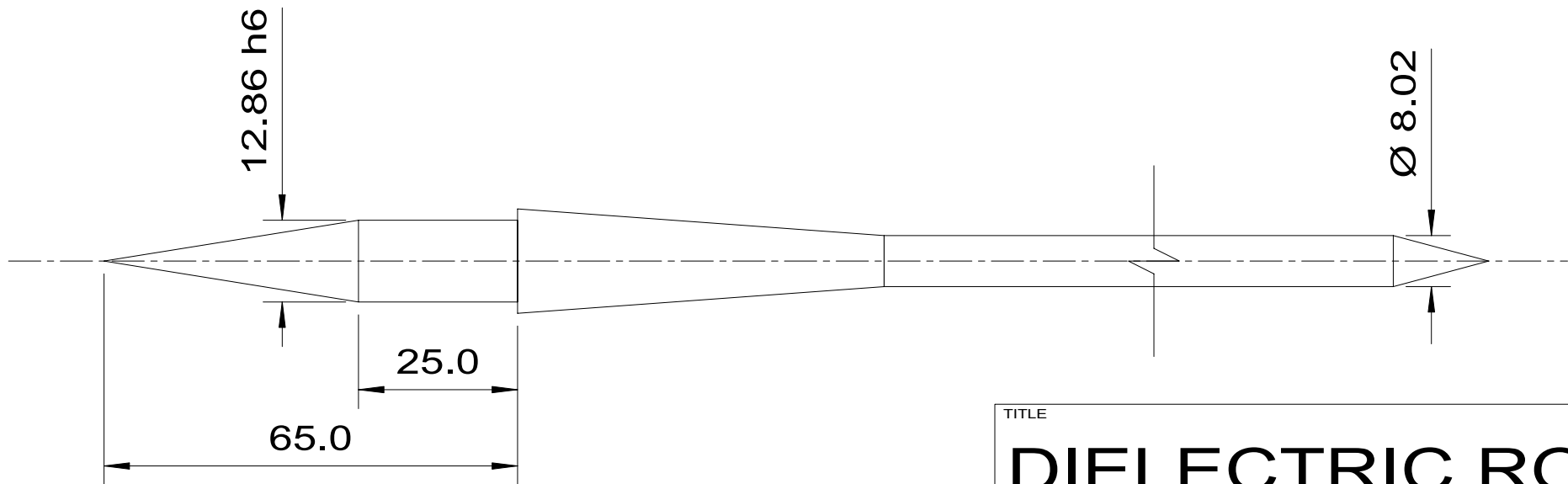
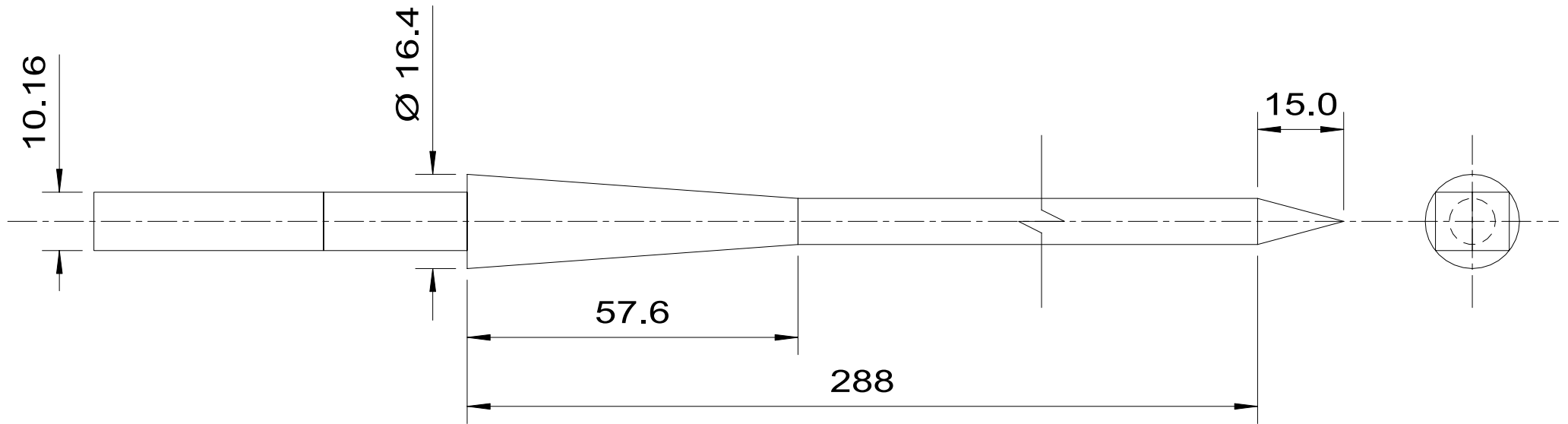
$$f_{c,mn} = \frac{1}{2\sqrt{\mu_1\epsilon_1}} \sqrt{\left(\frac{m}{a}\right)^2 + \left(\frac{n}{b}\right)^2} \Rightarrow f_{c,10} = 7.291\text{GHz}.$$

The empty waveguide section is matched to the reduced-sized filled section by tapering both the dielectric and the waveguide walls in the H-plane. The taper length is slightly longer than the TE₁₀ empty waveguide wavelength (i.e. 37mm) at the design frequency. The length of the reduced-sized filled waveguide section corresponds to one TE₁₀ wavelength in this section (i.e. 25mm). This length is sufficient to significantly reduce the amplitude of decaying higher order modes introduced by the taper discontinuities. The formula for calculating the wavelength in a rectangular waveguide is

$$\lambda_{c,mn} = \frac{2\pi}{\sqrt{k_1^2 - \left(\frac{m\pi}{a}\right)^2 - \left(\frac{n\pi}{b}\right)^2}},$$

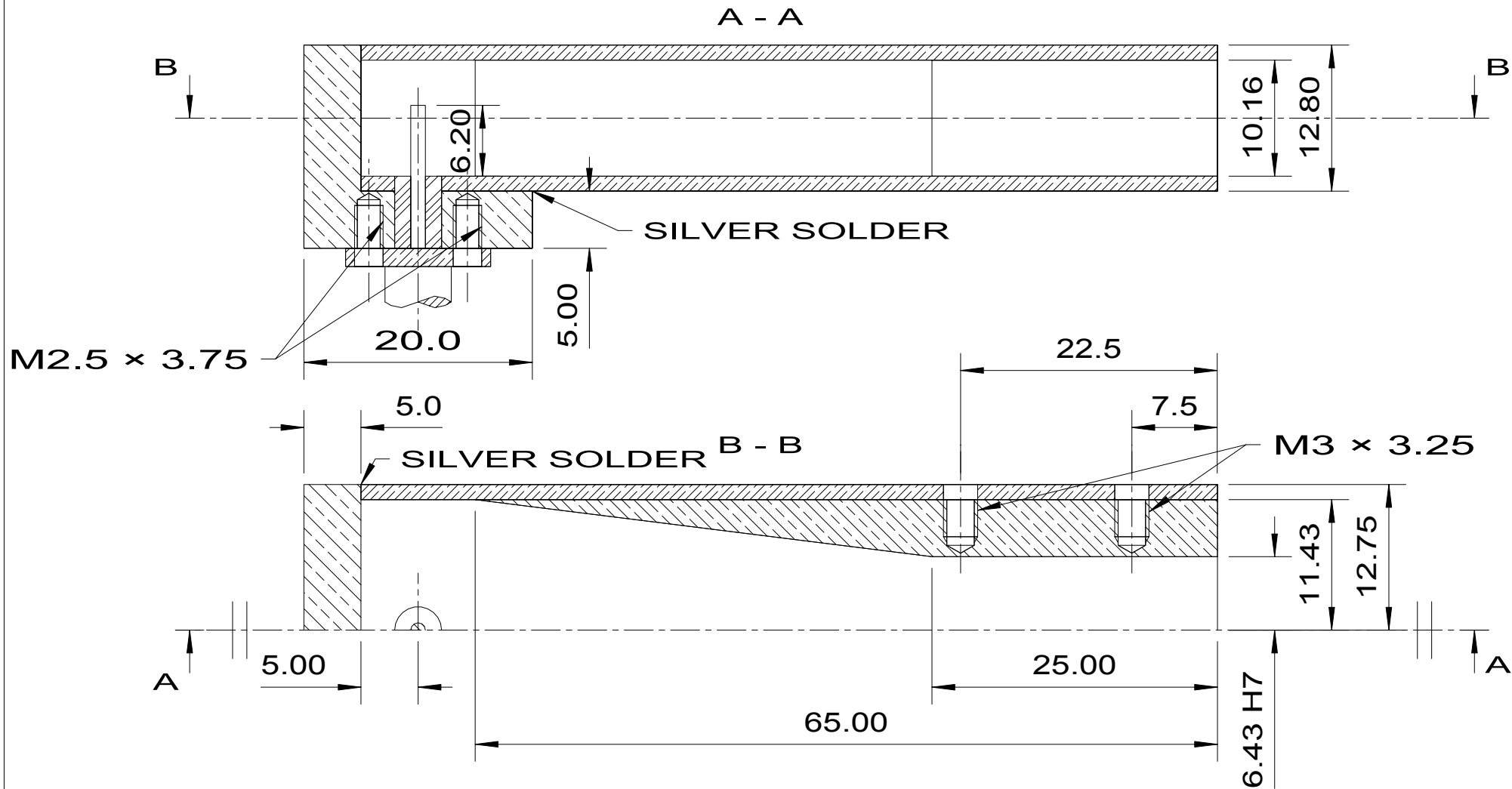
where $k_1^2 = \omega^2\mu_1\epsilon_1$.

Power is coupled into the waveguide by means of a probe connected to an SMA coaxial connector (Suhner type 13 SMA-50-0-53). By choosing the proper probe length, probe radius and short-circuit position, the input impedance can be made to equal the characteristic impedance Z_c of the input coaxial transmission line over a fairly broad frequency range and load impedance range. Unfortunately, very little design data are available in literature. However, Collin [7, pp. 471-483] has analysed the probe coax-to-waveguide adaptor by employing the method of moments. According to his simulation results, a probe with a radius of 0.64mm, 6.2mm long and a short-circuit positioned at 5mm from the centre of the probe should do fine.



MATERIAL: POLYSTYRENE

TITLE			
DIELECTRIC ROD			
K.U.LEUVEN Div. ESAT-TELEMIC			
	DRAWN BY	S. Y. STROOBANDT	DRAWING
	APPROVED BY		1 OF 2
DATE	29 APRIL 1997		ORIGINAL SCALE
			1:1
			DIMENSIONS IN MILLIMETERS



MATERIAL: BRASS

TITLE			
DIELECTRIC ROD			
K.U.LEUVEN Div. ESAT-TELEMIC			
	DRAWN BY	DRAWING	
	S. Y. STROOBANDT	2 OF 2	
	APPROVED BY	ORIGINAL SCALE	
		1:1	
	DATE	DIMENSIONS IN MILLIMETERS	
	29 APRIL 1997		

3 Measurements

3.1 Measurement Procedures

Three types of measurements have been performed:

- an input reflectivity measurement,
- a frequency swept measurement of the maximum (end-fire) gain,
- radiation pattern measurements in the E- and the H-plane.

3.1.1 Measuring the Input Reflectivity

For the input reflectivity measurement, the antenna is pointed to a sheet of broad-band absorbing material. The input reflectivity S_{11} is then measured by means of an HP 8510 vector network analyser, which has been calibrated beforehand using an SMA calibration kit. A load-open-short (LOS) calibration cancels out the effects of the tracking error, source mismatch and directivity error at the reference plane.

3.1.2 Phase Error in Far-Field Measurements

The antenna is installed in the indoor anechoic chamber for the gain and radiation pattern measurements. Only the far field (i.e. with infinite separation between the transmit and receive antennas) radiation patterns and gain are of real interest to the antenna engineer. However, in the anechoic chamber, the distance between the transmit antenna and the antenna under test (AUT) is only about 7.3m. An estimate for the magnitude of the phase error that results from this finite separation distance between the antennas can be obtained as follows. The effective aperture of the AUT is [8, p. 47]

$$A_e = \frac{G_{\max} \lambda_0^2}{4\pi} = 6.612 \cdot 10^{-3} \text{m}^2.$$

This corresponds to an equivalent diameter D

$$\frac{\pi D^2}{4} = A_e \Rightarrow D = \sqrt{\frac{4A_e}{\pi}} = 91.76 \text{mm}.$$

The calculated equivalent diameter D is larger than minimum array element separation distance which corresponds to the -12dB contour around the dielectric rod antenna (see [5, p. 18]).

For a maximum tolerable phase error of 5° , the distance between the transmit antenna and the AUT should be at least [8, pp. 809-810]

$$9 \frac{D^2}{\lambda_0} = 2.629 \text{m}.$$

A separation distance of 7.3m will therefore result in a qualitative measurement with a phase error substantially smaller than 5° .

3.1.3 Gain and Radiation Pattern Measurements

A schematic diagram of the complete indoor antenna test system can be found in reference [9], complete with an explanation of the function of each component. However, reference [9] fails to give any information on calibration procedures. This very important matter will be discussed here.

A standard gain horn (SGH) serves as calibration standard. The boresite gain of this antenna is guaranteed and tabulated by its manufacturer at a number of frequencies.

For a frequency swept maximum gain measurement, it suffices to do a measurement with the SGH first. A table of offset values can then be calculated from this measurement and the tabulated gain values of the SGH. The gain of the actual AUT can easily be obtained by adding the offset values to the measured gain values of the AUT.

The same calibration method is used for the radiation pattern measurements. However, one should take care that this calibration is performed for both the E-plane sweep and the H-plane sweep measurements! In this context, it is important to know that the anechoic chamber does not show any vertical-to-horizontal symmetry and that both the transmit antenna and the AUT are rotated by means of a polarization rotor to switch from E-plane to H-plane measurements.

3.2 Results

A plot of the measured input reflectivity is given in Figure 6. The input reflectivity remains below -10dB from 9.55GHz to 12GHz. If the input reflectivity is allowed to go up to -9.375dB, the lower end of the matched frequency band further drops to 8.92GHz, which corresponds to a matching bandwidth of 3.08GHz! However, as will be shown in a moment, this does not imply that the antenna remains useful over this whole bandwidth.

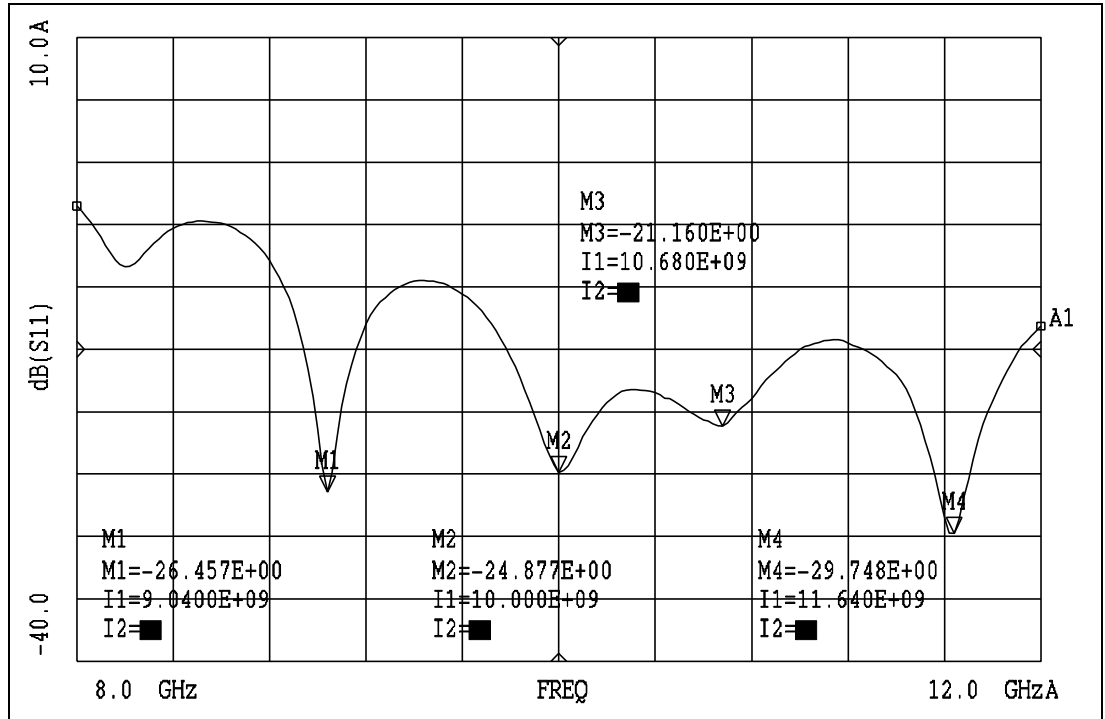


Figure 6: Absolute value of the antenna input reflectivity S_{11}

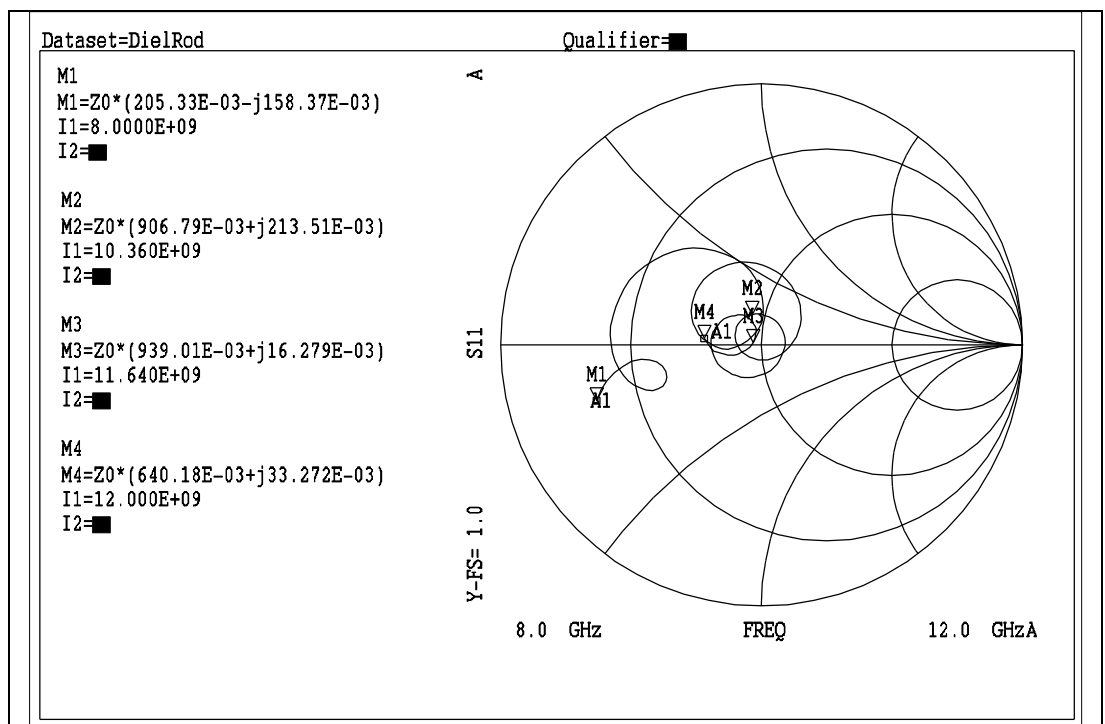


Figure 7: Smith chart of S_{11}

Figure 8 shows the results of a frequency swept maximum gain measurement. Maximum end-fire gain (20.5dBi) is obtained at 11.64GHz, the very frequency at which the input reflectivity is at its lowest. However, a local maximum for the end-fire gain (17.9dBi) can be discerned at 10.36GHz, which is near the design frequency of 10.4GHz. Figure 8 also explains why the useful gain bandwidth is usually smaller than the input impedance match bandwidth.

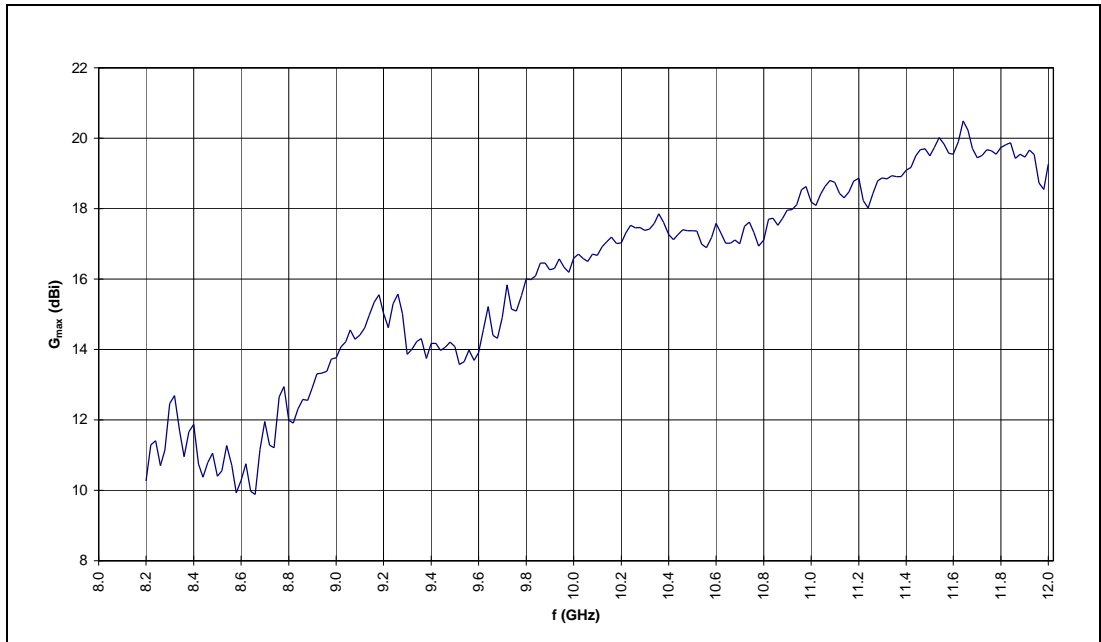


Figure 8: Maximum antenna gain as a function of frequency

E-plane and H-plane radiation patterns at 10.36GHz and 11.64GHz are given on the following pages.

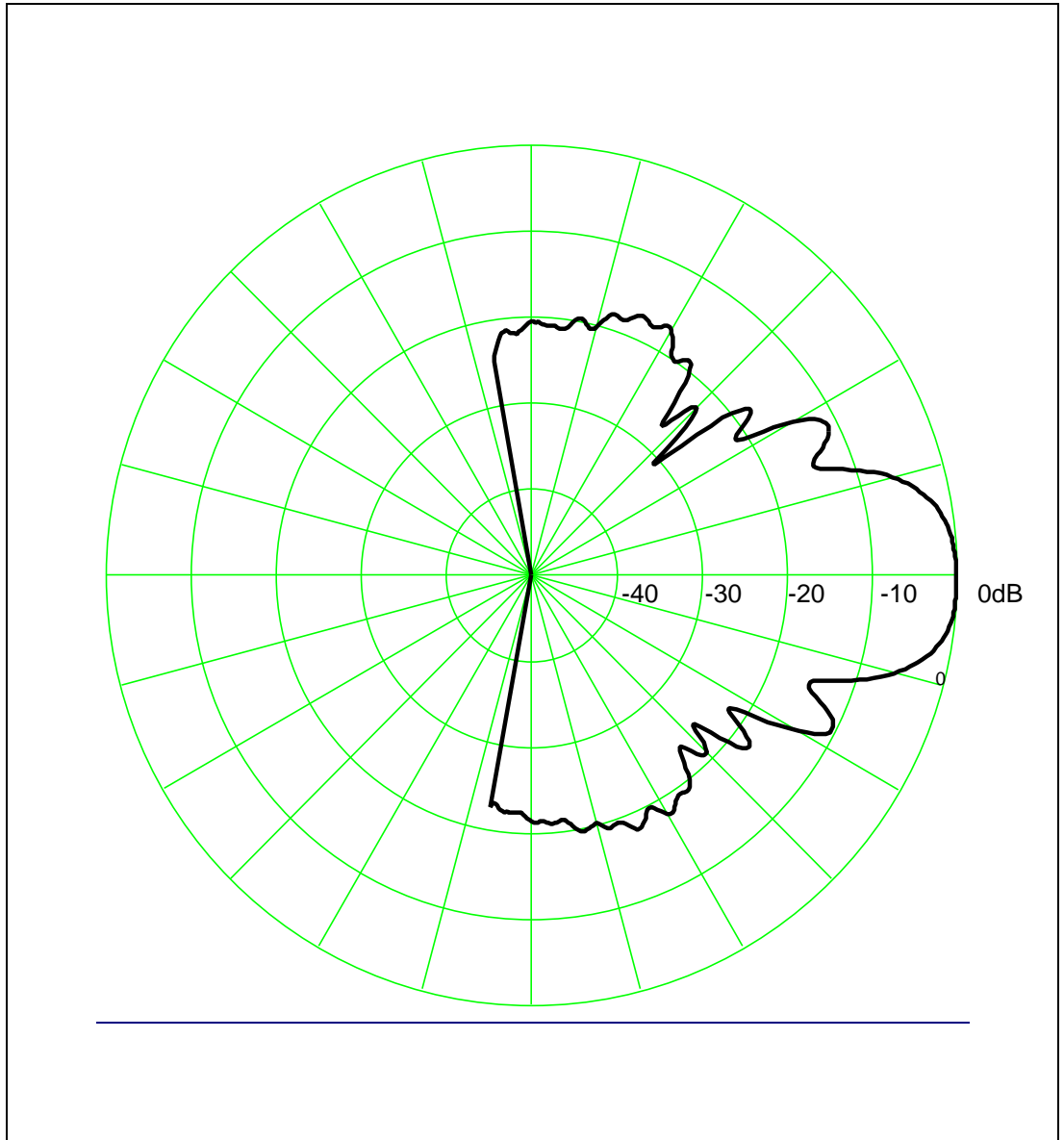


Figure 9: E-plane radiation pattern at 10.360GHz; $G_{\max} = 17.9\text{dBi}$

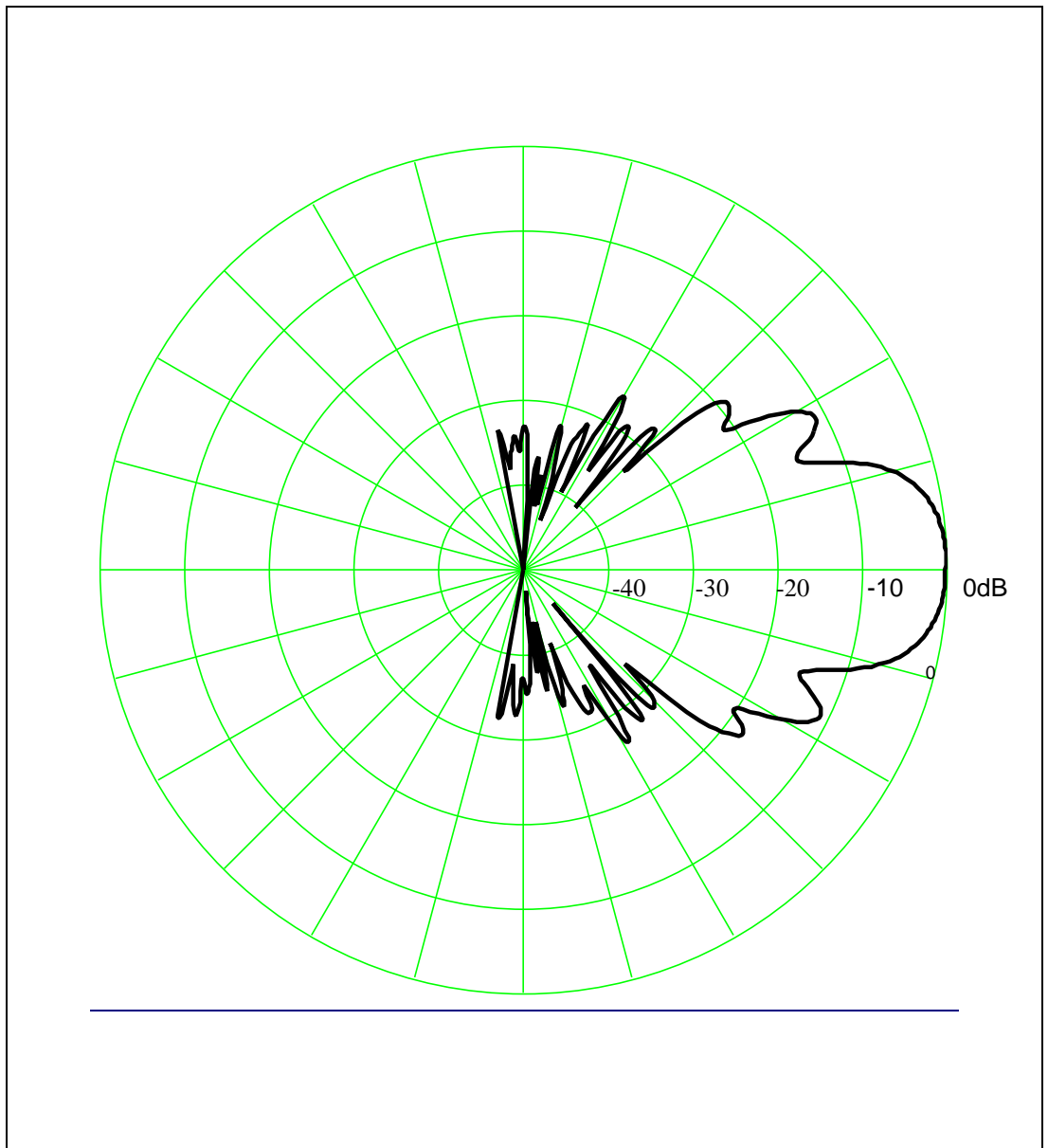


Figure 10: H-plane radiation pattern at 10.360GHz; $G_{\max} = 17.9\text{dBi}$

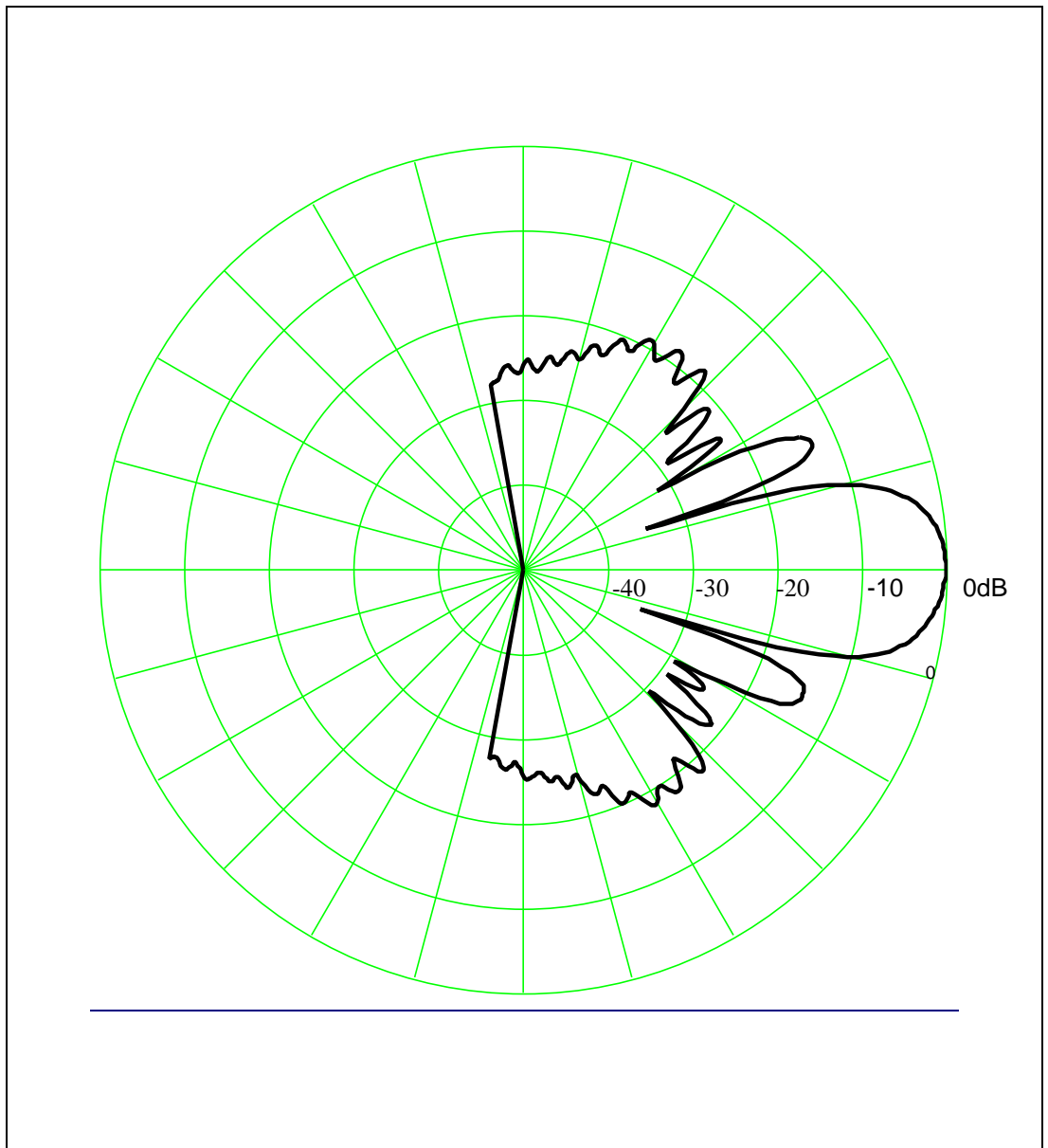


Figure 11: E-plane radiation pattern at 11.640GHz; $G_{\max} = 20.5\text{dBi}$

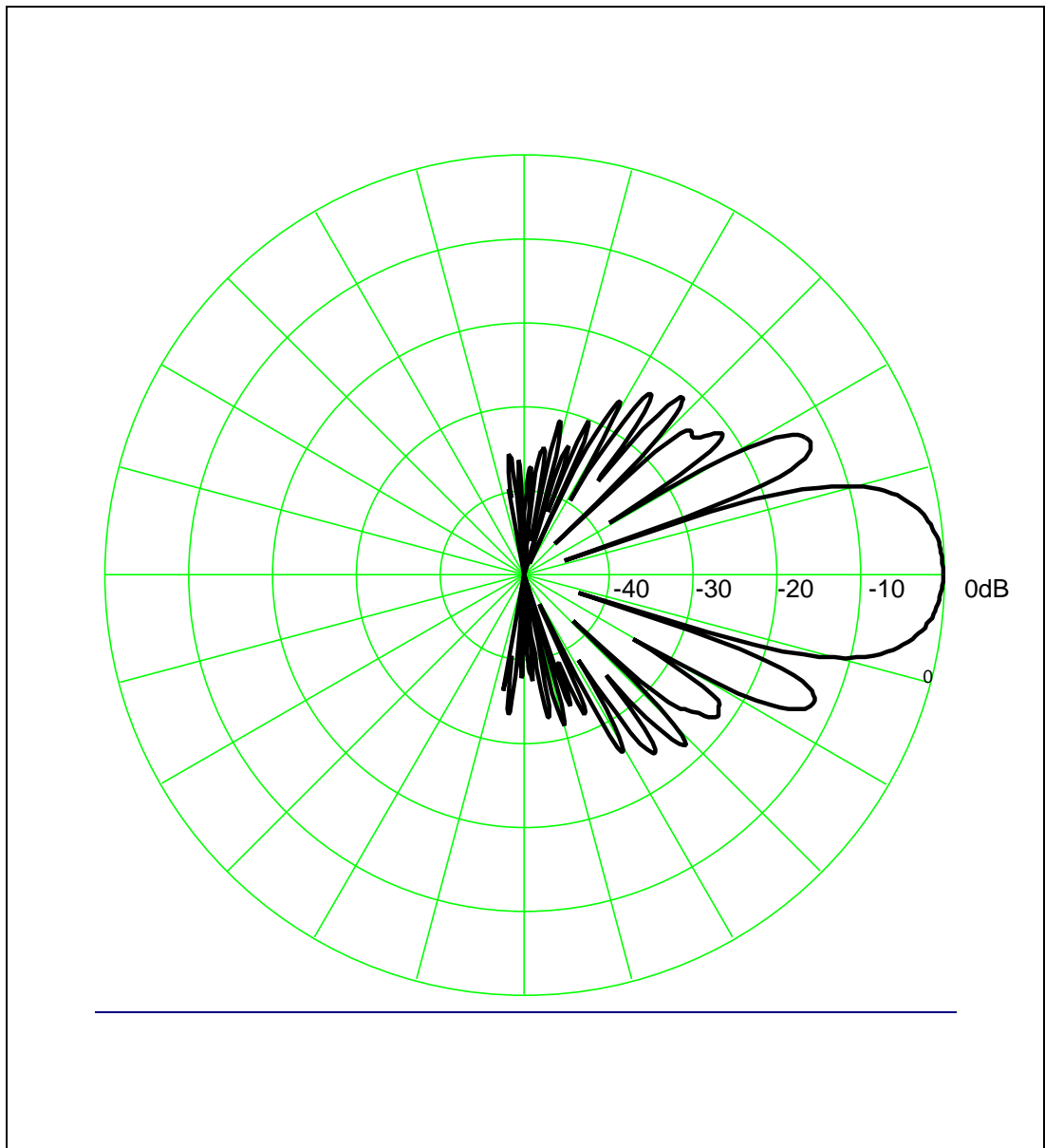


Figure 12: H-plane radiation pattern at 11.640GHz; $G_{\max} = 20.5\text{dBi}$

Note that the sidelobe level is considerably lower in the H-plane for both frequencies. This suggests that the sidelobes at higher angles (above 30°) must be due to the radiation from the rectangular waveguide feed.

Design tips for minimum sidelobe level, minimum beamwidth and broad pattern bandwidth are given in [5, pp. 14-16].

3.3 Areas for Improvement

3.3.1 Reverse Engineering

The predicted end-fire gain of 20dBi was not obtained at the desired frequency (10.4GHz). However, the maximum gain exceeded 20dBi by half a dB at 11.64GHz. This is most probably the result of not knowing what the value of the p factor should be in equation (4). The problem would not have occurred if the transition from feed to antenna structure could be modelled and the efficiency of excitation predicted (see for example [1]).

The parameters of a second prototype can easily be obtained by assuming that p varies only little with frequency. This process of reverse engineering would ultimately result in the correct value for p and hence maximum gain at the desired frequency.

At 11.64GHz, the free space wavelength is $\lambda_0 = 25.76\text{mm}$. The relative antenna length is $\ell / \lambda_0 = 11.18$. The relative rod diameter is $2a / \lambda_0 = 0.311$. The relative phase velocity of the HE_{11} surface wave mode is obtained from Figure 5: $\lambda_0 / \lambda_z = 1.020$.

The actual value of the factor p can now be calculated from equation 4:

$$p = \frac{\lambda_0}{\ell \left(\frac{\lambda_0}{\lambda_z} - 1 \right)} = 4.472.$$

This is not much different from the original value: $p = 4.545$.

3.3.2 Increased Gain

An increase in gain by 3dB can be realized by employing a surface wave antenna in a backfire configuration. In this configuration, a surface wave antenna is terminated by a flat circular conducting plate, which reflects the propagating surface wave back to the feed where it radiates into space. Design guidelines are given in [5, p. 14].

Easier and cheaper to build than a parabolic dish, the backfire antenna might be competitive for gains up to 25dBi provided sidelobes do not have to be very low.

The retina of a cat's eye is an array of backfire dielectric rod and cone antennas. This explains why the retina of the cat is highly reflective, unlike the human retina. Also, cats have better night vision than humans.

4 Conclusions

Dielectric rod antennas provide significant performance advantages and are a low cost alternative to free space high-gain antennas at millimeter-wave frequencies and the higher end of the microwave band. The fundamental working principles of this type of antenna were explained and guidelines were given for a maximum gain design. These were applied to an X-band antenna design which resulted in a maximum end-fire gain of 20.5dBi for an antenna length of $11.18\lambda_0$. E- and H-plane radiation patterns were measured as well, revealing high sidelobe levels, especially in the E-plane. This is about the only fundamental disadvantage of the dielectric rod antenna. However, some end-fire gain and main beam sharpness could be sacrificed to reduce the level of the sidelobes. The tapered dielectric in waveguide feed configuration proved to be well matched over an extremely wide band; over 3GHz. The pattern bandwidth depends on the intended application of the antenna, but is in general also quite large. Not knowing the surface wave excitation efficiency of the feed was the only difficulty encountered during the design process. As a result, the maximum end-fire gain was achieved at a frequency different from the design frequency. This problem would not have existed if a computer code was available to model the transition from feed to antenna.

5 References

- [1] B. Toland, C. C. Liu and P. G. Ingerson, "Design and analysis of arbitrarily shaped dielectric antennas," *Microwave Journal*, May 1997, pp. 278-286
- [2] J. D. Kraus, *Electromagnetics*, McGraw-Hill, 4th Ed., 1991, pp. 697-698
- [3] F. Werblin, A. Jacobs and J. Teeters, "The computational eye," *IEEE Spectrum*, May 1996, pp. 30-37
- [4] J. Wyatt and J. Rizzo, "Ocular implants for the blind," *IEEE Spectrum*, May 1996, pp. 47-53
- [5] F. J. Zucker, "Surface-wave antennas," Chapter 12 in R. C. Johnson, *Antenna Engineering Handbook*, McGraw-Hill, 3rd Ed., 1993
- [6] H. W. Ehrenspeck and H. Pöhler, "A new method for obtaining maximum gain from Yagi antennas," *IRE Transactions on Antennas and Propagation*, Vol. AP-7, 1959, p. 379
- [7] R. E. Collin, *Field Theory of Guided Waves*, IEEE Press, 2nd Ed., 1991
- [8] J. D. Kraus, *Antennas*, McGraw-Hill, 2nd Ed., 1988
- [9] "Antenna measurements, Manual pattern measurements using the HP 8510B," Hewlett Packard, Product Note 8510-11, 1987

Appendix A: Hertz Potentials

A.1 Hertz's Wave Equation for Source Free Homogeneous Linear Isotropic Media

Assuming $e^{j\omega t}$ time dependence, *Hertz's wave equation* for a source free homogeneous linear isotropic medium, independent of the coordinate system, is [1, p. 729]

$$\nabla^2 \vec{\Pi} + k^2 \vec{\Pi} = 0 \quad (1)$$

where $\nabla^2 \vec{v} \equiv \vec{\nabla}(\vec{\nabla} \cdot \vec{v}) - \vec{\nabla} \times \vec{\nabla} \times \vec{v}$ (\vec{v} is any vector) [1, p. 95], [2, p. 25]

and $k^2 = -j\omega\mu(\sigma + j\omega\epsilon) = \epsilon\mu\omega^2 - j\omega\mu\sigma$.

(k is *the complex wave number* of the surrounding medium.)

Hertz's wave equation for source free homogeneous linear isotropic media (1) has two types of independent solutions: $\vec{\Pi}_e$ and $\vec{\Pi}_m$.

These result in independent sets of *E-type waves*

$$\vec{H} = (\sigma + j\omega\epsilon)\vec{\nabla} \times \vec{\Pi}_e, \quad (2a)$$

$$\vec{E} = k^2 \vec{\Pi}_e + \vec{\nabla}(\vec{\nabla} \cdot \vec{\Pi}_e), \quad (2b)$$

and *H-type waves*, respectively [1, p. 729]

$$\vec{E} = -j\omega\mu \vec{\nabla} \times \vec{\Pi}_m, \quad (3a)$$

$$\vec{H} = k^2 \vec{\Pi}_m + \vec{\nabla}(\vec{\nabla} \cdot \vec{\Pi}_m). \quad (3b)$$

Note that throughout this text, permittivity ϵ will be treated as a complex quantity with two distinct loss contributions [3]

$$\epsilon = \epsilon' - j\epsilon'' - j\frac{\sigma}{\omega}$$

where $-j\epsilon''$ is the loss contribution due to molecular relaxation

and $-j\frac{\sigma}{\omega}$ is the conduction loss contribution. (The conductivity σ is measured at DC.)

However, in practice it is not always possible to make this distinction. This is often the case with metals and good dielectrics. In those cases all losses can be treated as though being entirely due to conduction or molecular relaxation, respectively.

Above relations follow from

$$\vec{\nabla} \times \vec{H} = j\omega\vec{D} + \vec{J} = j\omega(\epsilon' - j\epsilon'')\vec{E} + \sigma\vec{E}.$$

The loss tangent of a dielectric medium is defined by

$$\tan\delta \equiv \frac{\omega\epsilon'' + \sigma}{\omega\epsilon'}.$$

Permeability μ has only one loss contribution due to hysteresis: $\mu = \mu' - j\mu''$.

A.2 Hertz's Wave Equation in Orthogonal Curvilinear Coordinate Systems with Two Arbitrary Scale Factors

Consider a right-hand orthogonal curvilinear coordinate system with *curvilinear coordinates* (u_1, u_2, u_3) . Scale factor h_1 equals one and scale factors h_2 and h_3 can be chosen arbitrary.

(A detailed explanation of what curvilinear coordinates and scale factors are, can be found in [2, pp. 38-59] and [4, pp. 124-130], together with definitions of gradient, divergence, curl and Laplacian for such coordinate systems.)

Hertz's vector wave equation for source free homogeneous linear isotropic media (1) can be reduced to a scalar wave equation [1, pp. 729-730] by making use of the definitions given in [2, pp. 49-50]

$$\frac{\partial^2 \Pi}{\partial u_1^2} + \frac{1}{h_2 h_3} \frac{\partial}{\partial u_2} \left(\frac{h_3}{h_2} \frac{\partial \Pi}{\partial u_2} \right) + \frac{1}{h_2 h_3} \frac{\partial}{\partial u_3} \left(\frac{h_2}{h_3} \frac{\partial \Pi}{\partial u_3} \right) + k^2 \Pi = 0 \quad (4)$$

$$\text{with } \vec{\Pi} = \Pi(u_1, u_2, u_3) \vec{e}_1. \quad (5)$$

\vec{e}_1 is in the u_1 -direction.

The field components of the E-type waves are obtained by introducing (5) into (2a+b)

$$\begin{aligned} E_1 &= k^2 \Pi_e + \frac{\partial^2 \Pi_e}{\partial u_1^2}; \quad H_1 = 0, \\ E_2 &= \frac{1}{h_2} \frac{\partial^2 \Pi_e}{\partial u_1 \partial u_2}; \quad H_2 = \frac{(\sigma + j\omega\epsilon)}{h_3} \frac{\partial \Pi_e}{\partial u_3}, \\ E_3 &= \frac{1}{h_3} \frac{\partial^2 \Pi_e}{\partial u_1 \partial u_3}; \quad H_3 = -\frac{(\sigma + j\omega\epsilon)}{h_2} \frac{\partial \Pi_e}{\partial u_2}. \end{aligned} \quad (6)$$

The field components of the H-type waves are obtained by introducing (5) into (3a+b)

$$\begin{aligned} H_1 &= k^2 \Pi_m + \frac{\partial^2 \Pi_m}{\partial u_1^2}; \quad E_1 = 0, \\ H_2 &= \frac{1}{h_2} \frac{\partial^2 \Pi_m}{\partial u_1 \partial u_2}; \quad E_2 = -\frac{j\omega\mu}{h_3} \frac{\partial \Pi_m}{\partial u_3}, \\ H_3 &= \frac{1}{h_3} \frac{\partial^2 \Pi_m}{\partial u_1 \partial u_3}; \quad E_3 = \frac{j\omega\mu}{h_2} \frac{\partial \Pi_m}{\partial u_2}. \end{aligned} \quad (7)$$

As can be seen from (7) and (8), E-type waves have no H-component in the x_1 -direction, whereas H-type waves have no E-component in that direction. By choosing appropriate values for h_2 and h_3 , expressions for the field components in Cartesian, cylindrical (including parabolic and elliptic) and even spherical coordinate systems can be obtained.

The more general case with three arbitrary scale factors gives rise to an insoluble set of interdependent equations [2, pp. 50-51].

A.3 Hertz's Wave Equation in a Circular Cylindrical Coordinate System

In a cylindrical coordinate system, the scale factors are generally different from one, except for the scale factor associated with the symmetry axis, usually called the z-axis. In order to apply expression (4), the scale factor h_1 should equal one. Therefore, let $u_1 = z$.

The special case of a right-hand *circular* cylindrical coordinate system (r, ϕ, z) gives $u_1 = z$; $u_2 = r$ and $u_3 = \phi$. (8)

The differential line element $d\ell$ in a circular cylindrical coordinate system (r, ϕ, z) is [5]

$$d\ell = \sqrt{dr^2 + r^2d\phi^2 + dz^2}.$$

The scale factors are hence [4, p. 124]

$$h_1 = \left| \frac{\partial \ell}{\partial z} \right| = 1; \quad h_2 = \left| \frac{\partial \ell}{\partial r} \right| = 1 \quad \text{and} \quad h_3 = \left| \frac{\partial \ell}{\partial \phi} \right| = r. \quad (9)$$

Substitute (8) and (9) into (4) to get

$$\frac{\partial^2 \Pi}{\partial z^2} + \frac{1}{r} \frac{\partial}{\partial r} \left(r \frac{\partial \Pi}{\partial r} \right) + \frac{1}{r} \frac{\partial}{\partial \phi} \left(\frac{1}{r} \frac{\partial \Pi}{\partial \phi} \right) + k^2 \Pi = 0 \quad (10)$$

$$\text{with } \vec{\Pi} = \Pi(z, r, \phi) \vec{e}_z. \quad (11)$$

Propagation in cylindrical symmetric transmission lines occurs in one direction only, which is usually along the z-axis. This means that the expression for the Hertz vector potentials simplifies to

$$\vec{\Pi} = F(r, \phi) e^{-j\beta_z z} \vec{e}_z.$$

Since $\frac{\partial^2 \Pi}{\partial z^2} = -\beta_z^2 \Pi$, Hertz's scalar wave equation (10) becomes

$$\frac{1}{r} \frac{\partial}{\partial r} \left(r \frac{\partial \Pi}{\partial r} \right) + \frac{1}{r} \frac{\partial}{\partial \phi} \left(\frac{1}{r} \frac{\partial \Pi}{\partial \phi} \right) + s^2 \Pi = 0 \quad (12)$$

$$\text{where } s^2 = k^2 - \beta_z^2 = \epsilon \mu \omega^2 - j \omega \mu \sigma - \beta_z^2. \quad (13)$$

Solutions to (12) can readily be found by separation of the variables. Namely, let $\Pi = R(r)\Phi(\phi)e^{-j\beta_z z}$. (14)

Substituting (14) into (12) and dividing by (14) results in [1, p. 739]

$$\frac{1}{R} \left[\frac{1}{r} \frac{d}{dr} \left(r \frac{dR}{dr} \right) \right] + \frac{1}{\Phi} \left[\frac{1}{r} \frac{d}{d\phi} \left(\frac{1}{r} \frac{d\Phi}{d\phi} \right) \right] + s^2 = 0. \quad (15)$$

Multiplying (15) by r^2 gives

$$\frac{r}{R} \frac{d}{dr} \left(r \frac{dR}{dr} \right) + \frac{1}{\Phi} \frac{d^2 \Phi}{d\phi^2} + s^2 r^2 = 0. \quad (16)$$

Equation (16) can be separated using a separation constant n into

$$\frac{1}{\Phi} \frac{d^2 \Phi}{d\phi^2} = -n^2, \quad (17)$$

$$\frac{r}{R} \frac{d}{dr} \left(r \frac{dR}{dr} \right) + s_r^2 r^2 = n^2 \quad (18)$$

where $s_r^2 = s^2 = k^2 - \beta_z^2$.

Equation (17) is a linear homogeneous second order differential equation

$$\frac{d^2 \Phi}{d\phi^2} + n^2 \Phi = 0.$$

Solutions for Φ are of the form [4, p. 105]

$$\Phi = c_1 e^{+jn\phi} + c_2 e^{-jn\phi}, \text{ or equally,} \quad (19a)$$

$$\Phi = c_3 \cos(n\phi) + c_4 \sin(n\phi). \quad (19b)$$

Rewriting equation (18) results in an expression which can be recognized as Bessel's equation of order n [4, p. 106]

$$\frac{r}{R} \frac{d}{dr} \left(r \frac{dR}{dr} \right) + s_r^2 r^2 - n^2 = 0$$

$$\Rightarrow \frac{r}{R} \left(r \frac{d^2 R}{dr^2} + 1 \cdot \frac{dR}{dr} \right) + s_r^2 r^2 - n^2 = 0$$

$$\Rightarrow r^2 \frac{d^2 R}{dr^2} + r \frac{dR}{dr} + (s_r^2 r^2 - n^2) R = 0 \quad (20)$$

with $n \geq 0$.

Solutions to Bessel's equation of order n (20) are of the form [4, p. 106], [6, pp. 97-88]

$$R = c_5 J_n(s_r r) + c_6 Y_n(s_r r), \text{ or equally,} \quad (21a)$$

$$R = c_7 H_n^{(1)}(s_r r) + c_8 H_n^{(2)}(s_r r). \quad (21b)$$

These solutions are linearly independent only if n is a positive integer.

At this point, Hertz's scalar wave equation for circular cylindrical coordinate systems (12) solved. It suffices to substitute any form of (19) and (21) into (14) to obtain the Hertz potential solutions.

Substituting (8) and (14) into (6) gives the field components of the E-type waves expressed in terms of a Hertz potential [1, p.740]

$$\begin{aligned}
 E_z &= s_r^2 \Pi_e; \quad H_z = 0, \\
 E_r &= -j\beta_z \frac{\partial \Pi_e}{\partial r}; \quad H_r = \frac{(\sigma + j\omega\epsilon)}{r} \frac{\partial \Pi_e}{\partial \phi}, \\
 E_\phi &= -j\frac{\beta_z}{r} \frac{\partial \Pi_e}{\partial \phi}; \quad H_\phi = -(\sigma + j\omega\epsilon) \frac{\partial \Pi_e}{\partial r}.
 \end{aligned} \tag{22}$$

Likewise, substitute (8) and (14) into (7) to obtain the field components of the H-type waves

$$\begin{aligned}
 H_z &= s_r^2 \Pi_m; \quad E_z = 0, \\
 H_r &= -j\beta_z \frac{\partial \Pi_m}{\partial r}; \quad E_r = -j\frac{\omega\mu}{r} \frac{\partial \Pi_m}{\partial \phi}, \\
 H_\phi &= -j\frac{\beta_z}{r} \frac{\partial \Pi_m}{\partial \phi}; \quad E_\phi = j\omega\mu \frac{\partial \Pi_m}{\partial r}.
 \end{aligned} \tag{23}$$

A.4 References

- [1] K. Simonyi, *Theoretische Elektrotechnik*, Johann Ambrosius Barth, 10. Auflage, 1993, (in German)
- [2] J. A. Stratton, *Electromagnetic Theory*, McGraw-Hill, 1941
- [3] R. E. Collin, *Foundations for Microwave Engineering*, McGraw-Hill, 2nd Ed., 1992, p. 26
- [4] M. R. Spiegel, *Mathematical Handbook of Formulas and Tables*, Schaum's Outline Series, McGraw-Hill, 1968
- [5] Joseph A. Edminister, *Electromagnetics*, Schaum's Outline Series, McGraw-Hill, 2nd Ed., 1993, p. 5
- [6] R. E. Collin, *Field Theory of Guided Waves*, IEEE Press, 2nd Ed., 1991

Appendix B: Axial Surface Waves in Isotropic Media

B.1 Definition

An axial surface wave is a plane wave that propagates in the axial direction of a cylindrical interface of two different media without radiation.

Axial surface waves are plane waves because the phase remains constant along a plane perpendicular to the cylinder axis. They are also inhomogeneous because the field is not constant along surfaces of constant phase.

Sommerfeld was first to suggest the existence of axial surface waves in 1899. Goubau subsequently developed the idea in its application to a transmission line consisting of a coated metal wire[1]. With reference to this early research, the terms *Sommerfeld wave* and *Goubau wave* are sometimes used to denote an axial surface wave along a homogeneous rod and a coated metal wire, respectively. Axial surface waves are perhaps the most important type of surface waves with regard to practical applications [2]. Not only the Goubau line, but also the polyrod antenna supports axial surface waves (see Fig. B.1) [3].

Formulas for the electromagnetic field components in function of a Hertz potential were found in Section A.3. Moreover, (A.22) and (A.23) appear to imply that the longitudinal components of \vec{E} and \vec{H} are uncoupled, as is the case with the plane surface. However, in general, coupling of the longitudinal field components E_z and H_z is required by the boundary conditions of the electromagnetic field components [4, p.38]. This is in contrast with plane surface waves where the boundary conditions do not lead to coupling between the field components, resulting in mode solutions for which the longitudinal component of either \vec{E} or \vec{H} is zero. Cylindrical interfaces, however, not only support pure TE and TM axial surface wave modes but also modes for which both E_z and H_z are nonzero. These latter modes are in fact combinations of a TE and TM mode with a same β_z and are therefore called *hybrid modes*. They are designated as EH or HE modes, depending on whether the TM or the TE mode predominates, respectively [5, p. 721]. Representations of the field distributions of these different types of axial surface wave modes can be found at the end of this chapter.

B.2 Axial Surface Waves along a Dielectric and/or Magnetic Cylinder

The propagation of axial surface waves along a cylinder of dielectric and/or magnetic material (Fig. B.1) will be analysed in this section.

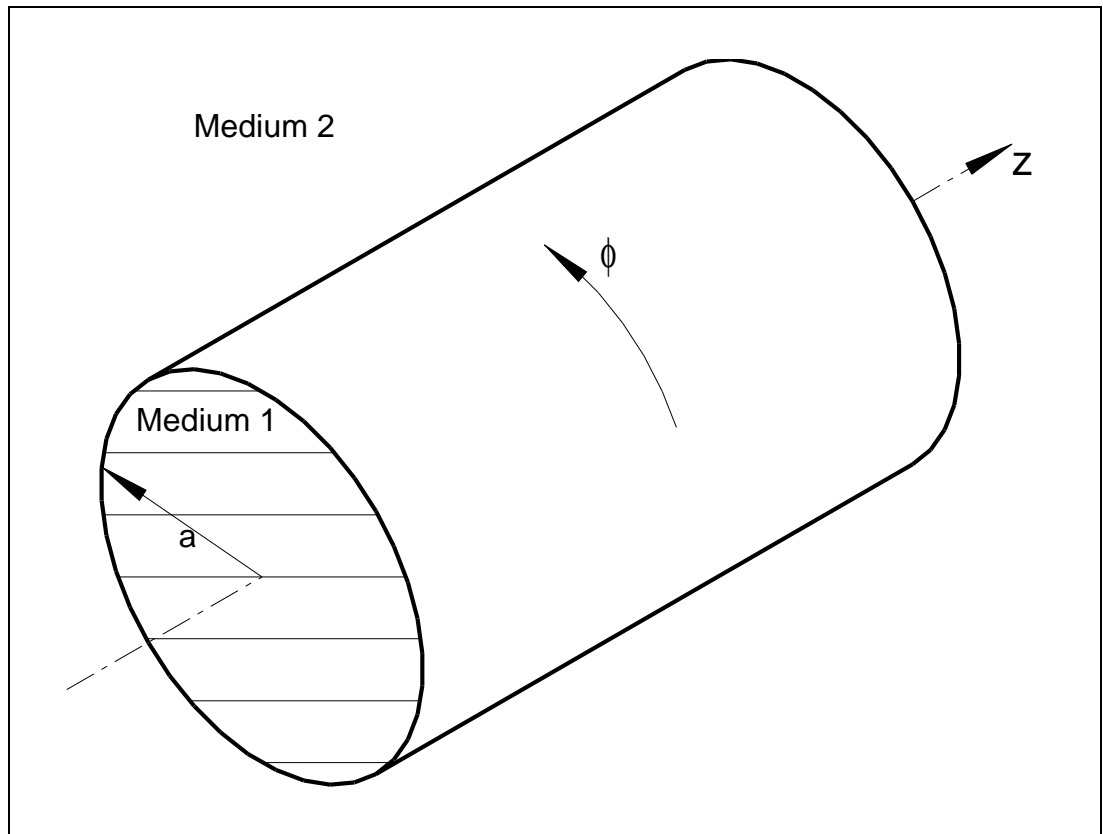


Figure B.1: A cylinder of dielectric and/or magnetic material

As was pointed out earlier, a cylindrical interface can support hybrid modes in addition to the pure TM and TE modes. In order to obtain hybrid mode solutions, equations (A.22) and (A.23) need to be evaluated simultaneously which makes the analysis more complex than the analysis of plane surface waves.

Suitable Hertz functions for medium 1 that can satisfy any boundary condition are

$$\Pi_{1e} = \sum_n A_n J_n(s_{r1}r) e^{-jn\phi} e^{-j\beta_z z} \quad \text{and} \quad (1)$$

$$\Pi_{1m} = \sum_n B_n J_n(s_{r1}r) e^{-jn\phi} e^{-j\beta_z z} \quad (2)$$

where n is a positive integer.

Because of their similarity to harmonic functions and their oscillatory behaviour, the Bessel functions of the first kind, J_n , may be interpreted here as standing waves in the r -direction. Solutions which contain Bessel functions of the second kind, Y_n , do not exist because these functions tend to $-\infty$ for $r = 0$.

Substituting (1) and (2) into (A.22) and (A.23), respectively, gives

$$E_{z1} = s_{r1}^2 \sum_n A_n J_n(s_{r1}r) e^{-jn\phi} e^{-j\beta_z z}, \quad (3a)$$

$$E_{r1} = \sum_n \left[-j\beta_z A_n s_{r1} J_n'(s_{r1}r) - \frac{n\omega\mu_1}{r} B_n J_n(s_{r1}r) \right] e^{-jn\phi} e^{-j\beta_z z}, \quad (3b)$$

$$E_{\phi 1} = \sum_n \left[-\frac{n\beta_z}{r} A_n J_n(s_{r1}r) + j\omega\mu_1 B_n s_{r1} J_n'(s_{r1}r) \right] e^{-jn\phi} e^{-j\beta_z z}, \quad (3c)$$

$$H_{z1} = s_{r1}^2 \sum_n B_n J_n(s_{r1}r) e^{-jn\phi} e^{-j\beta_z z}, \quad (3d)$$

$$H_{r1} = \sum_n \left[-j \frac{n(\sigma_1 + j\omega\epsilon_1)}{r} A_n J_n(s_{r1}r) - j\beta_z B_n s_{r1} J_n'(s_{r1}r) \right] e^{-jn\phi} e^{-j\beta_z z}, \quad (3e)$$

$$H_{\phi 1} = \sum_n \left[-(\sigma_1 + j\omega\epsilon_1) A_n s_{r1} J_n'(s_{r1}r) - \frac{n\beta_z}{r} B_n J_n(s_{r1}r) \right] e^{-jn\phi} e^{-j\beta_z z}. \quad (3f)$$

s_{r1} is chosen to equal the positive square root. Choosing the negative square root would have no effect in the results. Thus,

$$s_{r1} = \text{sign} \left[\text{Re} \left(\sqrt{k_1^2 - \beta_z^2} \right) \right] \sqrt{k_1^2 - \beta_z^2}. \quad (4)$$

The large argument approximations for J_n is [5, p. 835], [6, p. 228]

$$J_n(x) \approx \sqrt{\frac{2}{\pi x}} \cos \left(x - \frac{\pi}{4} - n \frac{\pi}{2} \right) \quad \text{for } |x| \gg 1. \quad (5)$$

Suitable Hertz functions for medium 2 that satisfy the boundary condition $\bar{\mathbf{E}} = \bar{\mathbf{H}} = \bar{\mathbf{0}}$ when $r \rightarrow +\infty$

are

$$\Pi_{2e} = \sum_n A_2 H_n^{(2)}(s_{r2}r) e^{-jn\phi} e^{-j\beta_z z} \quad \text{and} \quad (6)$$

$$\Pi_{2m} = \sum_n B_2 H_n^{(2)}(s_{r2}r) e^{-jn\phi} e^{-j\beta_z z}. \quad (7)$$

The reason why Hankel functions of the second kind are used instead of those of the first kind, becomes clear by looking at the large argument approximations of both function types. These are [5, p. 835] and [6, p. 228]

$$H_n^{(1)}(x) \approx \sqrt{\frac{2}{\pi x}} e^{j\left(x - \frac{\pi}{4} - n\frac{\pi}{2}\right)} \quad \text{and} \quad (8)$$

$$H_n^{(2)}(x) \approx \sqrt{\frac{2}{\pi x}} e^{-j\left(x - \frac{\pi}{4} - n\frac{\pi}{2}\right)}, \quad \text{both for } |x| \gg 1. \quad (9)$$

Comparing (8) and (9) with equivalent Hertz potentials for plane surface waves leads to the following conclusions:

- the use of Hankel functions of the second kind in Hertz potentials gives rise to proper axial wave solutions,
- whereas using Hankel functions of the first kind results in improper axial wave solutions.

It is also important to know that Hankel functions are undefined for negative pure real numbers [7]. However, when the imaginary part of the argument is nonzero, the real part can have any value. Hence, for proper axial waves

$$s_{r2} = \text{sign}\left[\text{Re}\left(\sqrt{k_2^2 - \beta_z^2}\right)\right] \sqrt{k_2^2 - \beta_z^2} \Rightarrow js_{r2} = \text{sign}\left[\text{Re}\left(\sqrt{\beta_z^2 - k_2^2}\right)\right] \sqrt{\beta_z^2 - k_2^2}, \quad (10a)$$

whereas for improper axial waves

$$s_{r2} = -\text{sign}\left[\text{Re}\left(\sqrt{k_2^2 - \beta_z^2}\right)\right] \sqrt{k_2^2 - \beta_z^2} \Rightarrow js_{r2} = -\text{sign}\left[\text{Re}\left(\sqrt{\beta_z^2 - k_2^2}\right)\right] \sqrt{\beta_z^2 - k_2^2}. \quad (10b)$$

Substituting (6) and (7) into (A.22) and (A.23), respectively, gives

$$\mathbf{E}_{z2} = s_{r2}^2 \sum_n A_2 H_n^{(2)}(s_{r2}r) e^{-jn\phi} e^{-j\beta_z z}, \quad (11a)$$

$$\mathbf{E}_{r2} = \sum_n \left[-j\beta_z A_2 s_{r2} H_n^{(2)}(s_{r2}r) - \frac{n\omega\mu_2}{r} B_2 H_n^{(2)}(s_{r2}r) \right] e^{-jn\phi} e^{-j\beta_z z}, \quad (11b)$$

$$\mathbf{E}_{\phi 2} = \sum_n \left[-\frac{n\beta_z}{r} A_2 H_n^{(2)}(s_{r2}r) + j\omega\mu_2 B_2 s_{r2} H_n^{(2)}(s_{r2}r) \right] e^{-jn\phi} e^{-j\beta_z z}, \quad (11c)$$

$$\mathbf{H}_{z2} = s_{r2}^2 \sum_n B_2 H_n^{(2)}(s_{r2}r) e^{-jn\phi} e^{-j\beta_z z}, \quad (11d)$$

$$\mathbf{H}_{r2} = \sum_n \left[-j \frac{n(\sigma_2 + j\omega\epsilon_2)}{r} A_2 H_n^{(2)}(s_{r2}r) - j\beta_z B_2 s_{r2} H_n^{(2)}(s_{r2}r) \right] e^{-jn\phi} e^{-j\beta_z z}, \quad (11e)$$

$$\mathbf{H}_{\phi 2} = \sum_n \left[-(\sigma_2 + j\omega\epsilon_2) A_2 s_{r2} H_n^{(2)}(s_{r2}r) - \frac{n\beta_z}{r} B_2 H_n^{(2)}(s_{r2}r) \right] e^{-jn\phi} e^{-j\beta_z z}. \quad (11f)$$

The tangential components of both \vec{E} and \vec{H} are continuous across the interface of two media. This yields the following expressions

$$E_{z1} = E_{z2} \text{ at } r = b \Rightarrow s_{r1}^2 J_n(s_{r1}b)A_1 - s_{r2}^2 H_n^{(2)}(s_{r2}b)A_2 = 0, \quad (12)$$

$$E_{\phi1} = E_{\phi2} \text{ at } r = b$$

$$\begin{aligned} \Rightarrow & -\frac{n\beta_z}{b} J_n(s_{r1}b)A_1 + j\omega\mu_1 s_{r1} J'_n(s_{r1}b)B_1 \\ & + \frac{n\beta_z}{b} H_n^{(2)}(s_{r2}b)A_2 - j\omega\mu_2 s_{r2} H_n^{(2)'}(s_{r2}b)B_2 = 0, \end{aligned} \quad (13)$$

$$H_{z1} = H_{z2} \text{ at } r = b \Rightarrow s_{r1}^2 J_n(s_{r1}b)B_1 - s_{r2}^2 H_n^{(2)}(s_{r2}b)B_2 = 0 \quad (14)$$

$$\text{and finally } H_{\phi1} = H_{\phi2} \text{ at } r = b$$

$$\begin{aligned} \Rightarrow & -(\sigma_1 + j\omega\epsilon_1) s_{r1} J'_n(s_{r1}b)A_1 - \frac{n\beta_z}{b} J_n(s_{r1}b)B_1 \\ & + (\sigma_2 + j\omega\epsilon_2) s_{r2} H_n^{(2)'}(s_{r2}b)A_2 + \frac{n\beta_z}{b} H_n^{(2)}(s_{r2}b)B_2 = 0. \end{aligned} \quad (15)$$

Equations (12), (13), (14) and (15) form a system of linear equations for the four unknown factors A_1, B_1, A_2 and B_2 . The system is homogeneous, hence for non-trivial solutions to exist, the coefficient determinant must be zero, that is

$$\begin{vmatrix} s_{r1}^2 J_n(s_{r1}b) & 0 & -s_{r2}^2 H_n^{(2)}(s_{r2}b) & 0 \\ -\frac{n\beta_z}{b} J_n(s_{r1}b) & j\omega\mu_1 s_{r1} J_n'(s_{r1}b) & \frac{n\beta_z}{b} H_n^{(2)}(s_{r2}b) & -j\omega\mu_2 s_{r2} H_n'^{(2)}(s_{r2}b) \\ 0 & s_{r1}^2 J_n(s_{r1}b) & 0 & -s_{r2}^2 H_n^{(2)}(s_{r2}b) \\ -(\sigma_1 + j\omega\epsilon_1) s_{r1} J_n'(s_{r1}b) & -\frac{n\beta_z}{b} J_n(s_{r1}b) & (\sigma_2 + j\omega\epsilon_2) s_{r2} H_n'^{(2)}(s_{r2}b) & \frac{n\beta_z}{b} H_n^{(2)}(s_{r2}b) \end{vmatrix} = 0. \quad (16)$$

Expanding the above determinant does not result in a simplified expression. Equation (16) may therefore be regarded as the dispersion equation of the axial surface waves propagating along a dielectric and/or magnetic cylinder. Solutions for the first three modes are given in Figure 5 on page 9 of this report.

However, it can be shown that, for $n=0$, (16) reduces to

$$\begin{aligned} & [(\sigma_1 + j\omega\epsilon_1) s_{r2} J_0'(s_{r1}b) H_0^{(2)}(s_{r2}b) - (\sigma_2 + j\omega\epsilon_2) s_{r1} J_0(s_{r1}b) H_0'^{(2)}(s_{r2}b)] \\ & \cdot [j\omega\mu_1 s_{r2} J_0'(s_{r1}b) H_0^{(2)}(s_{r2}b) - j\omega\mu_2 s_{r1} J_0(s_{r1}b) H_0'^{(2)}(s_{r2}b)] = 0. \end{aligned} \quad (17)$$

Also, for $n=0$, two distinct types of uncoupled modes are propagating. This can be seen from (3) and (11):

- H_z, E_r and E_ϕ belong to the field of TM modes,
- whereas E_z, H_r and H_ϕ make up the field of the TE modes.

The two factors at the left side of (17) correspond to the dispersion equation of the TM and TE modes, respectively. Equations (5), (8) and (9) also show that the field expressions of an axial surface wave tend toward those of a plane surface wave in the limit case of propagation along an electrically extremely thick cylinder.

B.3 Field Distribution of Axial Surface Waves along a Dielectric and/or Magnetic Cylinder

Because of the oscillatory behaviour of the Bessel functions J_n and Y_n , there will be m roots of equation (16) for any given n value. These roots are designated by β_{nm} and the corresponding modes are either TM_{0m} , TE_{0m} , EH_{nm} or HE_{nm} [4, p. 41-42].

As was already suggested towards the end of the previous section, TM and TE modes have no angular dependence, i.e. $n=0$.

The EH_{11} (or HE_{11}) mode is the fundamental mode; it has no low-frequency cutoff [6, p. 769].

Figure B.2 shows the transverse electric field vectors in medium 1 for the four lowest order modes.

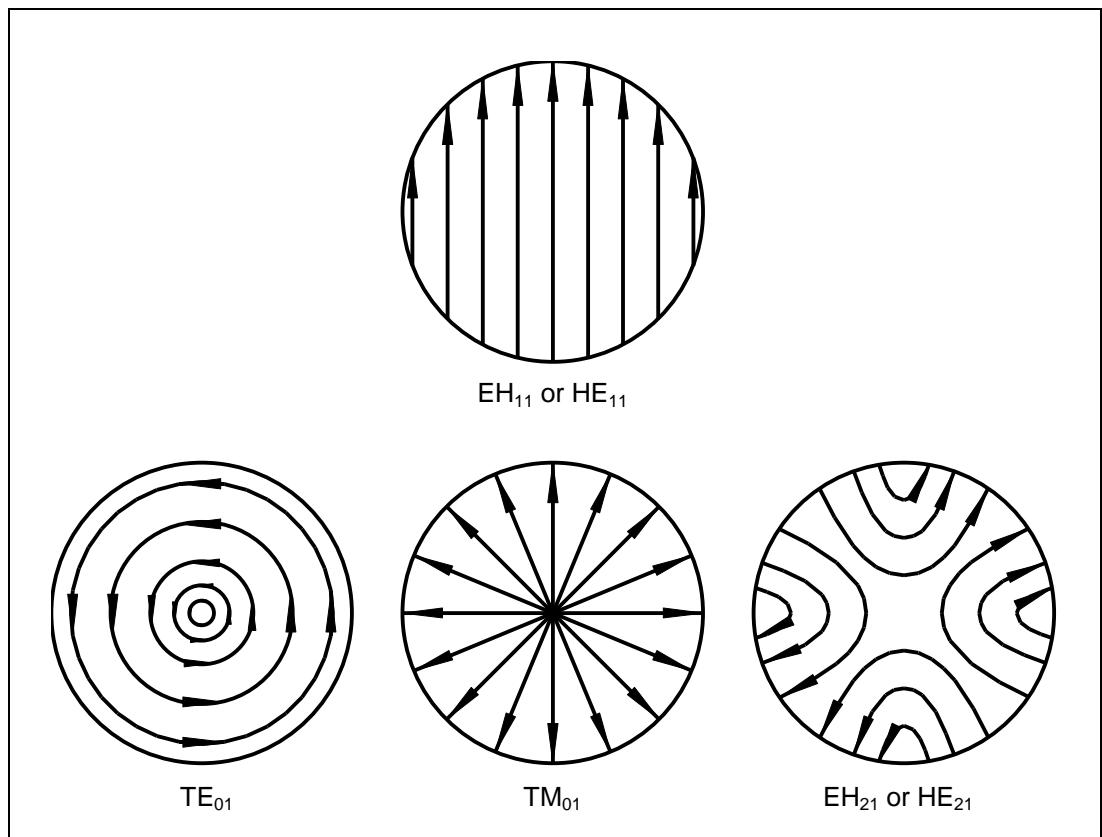


Figure B.2: The transverse electric field in medium 1 of the four lowest order modes

The external field of a TM axial surface wave is depicted in Figure B.3. For a TE wave the E- and H-fields are interchanged and one of the fields is reversed in sign.

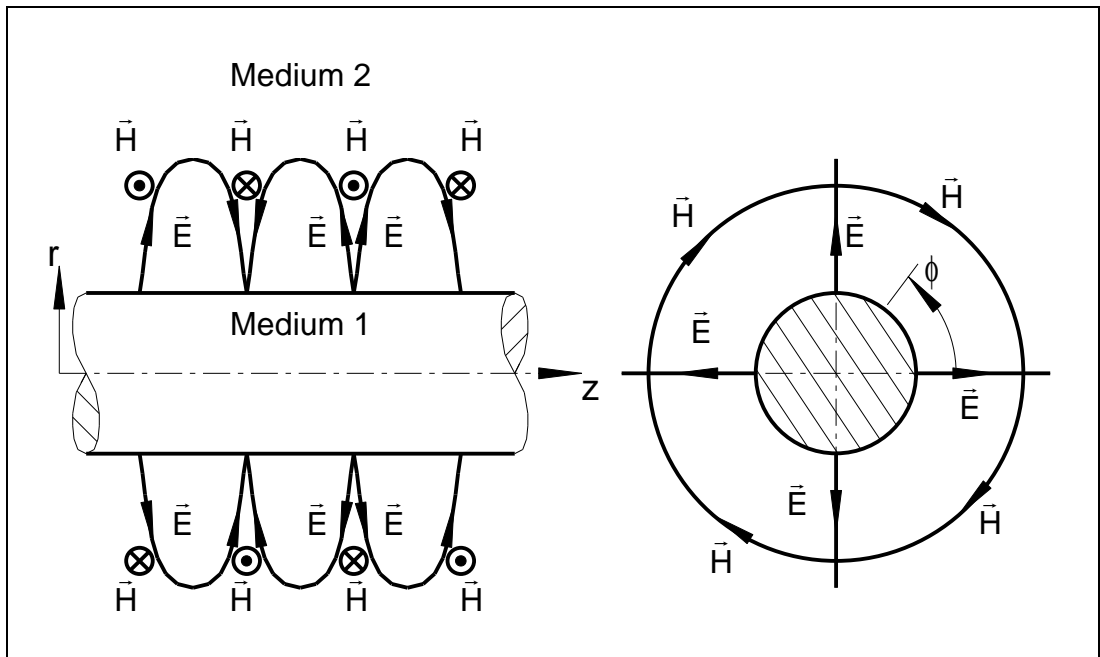


Figure B.3: The external field of a TM axial surface wave

B.4 References

- [1] H. M. Barlow and A. L. Cullen, "Surface waves," *Proceedings of the Institution of Electrical Engineers*, Vol. 100, Part III, No. 68, Nov. 1953, pp. 329-347
- [2] H. M. Barlow and J. Brown, *Radio Surface Waves*, Oxford University Press, 1962, p. 12
- [3] F. J. Zucker, "Surface-wave antennas," Chapter 12 in R. C. Johnson, *Antenna Engineering Handbook*, McGraw-Hill, 3rd Ed., 1993
- [4] G. Keiser, *Optical Fiber Communications*, McGraw-Hill, 2nd Ed.
- [5] R. E. Collin, *Field Theory of Guided Waves*, IEEE Press, 2nd Ed., 1991
- [6] K. Simonyi, *Theoretische Elektrotechnik*, Johann Ambrosius Barth, 10. Auflage, 1993, (in German)
- [7] M. Abramowitz and I. A. Stegun, *Handbook of Mathematical Functions*, Dover Publications, 1st Ed., 8th Printing, 1972, p. 359



